PNAS RESEARCH ARTICLE | BIOCHEMISTRY

Cryoelectron microscopy of Na^+,K^+-ATPase in the two E2P states with and without cardiotonic steroids

Ryuta Kanai (金井隆太)[a], Flemming Cornelius[b], Bente Vilsen[b], and Chikashi Toyoshima (豊島近)[a,1]

Contributed by Chikashi Toyoshima; received December 27, 2021; accepted March 3, 2022; reviewed by Kazuhiro Abe and Kathleen Sweadner

Cryoelectron microscopy (cryo-EM) was applied to Na^+,K^+-ATPase (NKA) to determine the structures of two E2P states, one ($E2P^{ATP}$) formed by ATP and Mg^{2+} in the forward reaction, and the other ($E2P^{Pi}$) formed by inorganic phosphate (P_i) and Mg^{2+} in the backward reaction, with and without ouabain or istaroxime, representatives of classical and new-generation cardiotonic steroids (CTSs). These two E2P states exhibit different biochemical properties. In particular, K^+-sensitive acceleration of the dephosphorylation reaction is not observed with $E2P^{Pi}$, attributed to the presence of a Mg^{2+} ion in the transmembrane cation binding sites. The cryo-EM structures of NKA demonstrate that the two E2P structures are nearly identical but Mg^{2+} in the transmembrane binding cavity is identified only in $E2P^{Pi}$, corroborating the idea that it should be denoted as $E2P^{Pi}{\cdot}Mg^{2+}$. We can now explain why the absence of transmembrane Mg^{2+} in $E2P^{ATP}$ confers the K^+ sensitivity in dephosphorylation. In addition, we show that ATP bridges the actuator (A) and nucleotide binding (N) domains, stabilizing the $E2P^{ATP}$ state; CTS binding causes hardly any changes in the structure of NKA, both in $E2P^{ATP}$ and $E2P^{Pi}{\cdot}Mg^{2+}$, indicating that the binding mechanism is conformational selection; and istaroxime binds to NKA, extending its aminoalkyloxime group deep into the cation binding site. This orientation is upside down compared to that of classical CTSs with respect to the steroid ring. Notably, mobile parts of NKA are resolved substantially better in the electron microscopy (EM) maps than in previous X-ray structures, including sugars sticking out from the β-subunit and many phospholipid molecules.

cryoelectron microscopy | sodium pump | Na^+,K^+-ATPase | cardiotonic steroids

Significance

The E2P state of Na^+,K^+-ATPase, in which the ATPase is phosphorylated and of low affinity to Na^+ with the extracellular gate opened, shows different biochemical properties depending on whether the phosphate is transferred from ATP in the forward reaction or from inorganic phosphate (P_i) in the backward reaction. We present here cryoelectron microscopy structures of Na^+,K^+-ATPase in the two E2P states, explaining their different biochemical properties established a half century ago. The new electron microscopy maps show previously unseen structural features, including unexpected binding modes of cardiotonic steroids, specific and medically important inhibitors of the ATPase, and stabilization by ATP of the E2P state.

In the E2P state of Na^+,K^+-ATPase (NKA) (Fig. 1), a conserved Asp residue in the phosphorylation domain (P domain) is phosphorylated and the transmembrane cation binding sites are open to the extracellular medium and have low affinity for Na^+ [for a recent general review on NKA, see, e.g., (1, 2)]. It has been pointed out that the E2P state of NKA made by ATP (denoted as $E2P^{ATP}$) in the forward direction in the reaction cycle and the E2P state of NKA made by inorganic phosphate (P_i) ($E2P^{Pi}$) in the backward direction are different (3–5). The differences have been attributed to the presence of a Mg^{2+} ion bound to one of the transmembrane cation binding sites in $E2P^{Pi}$ with a relatively high affinity (~0.5 mM dissociation constant) (3). A crystal structure of NKA in $E2P^{Pi}$, made with the stable phosphate analog BeF_3^- grown in the presence of ~100 mM Mg^{2+}, indeed showed a Mg^{2+} ion in the cation binding cavity between sites I and II (6). This Mg^{2+} binding site is located at a position similar to that in $E1{\cdot}Mg^{2+}$ of SERCA1a (7). Thus, it is more appropriate to denote $E2P^{Pi}$ as $E2P^{Pi}{\cdot}Mg^{2+}$ (6) and the Mg^{2+} binding site as site M.

Differences are manifested by three kinds of evidence: K^+ sensitivity in the dephosphorylation reaction ($E2P^{ATP} \rightarrow E2$ is accelerated by K^+ but $E2P^{Pi} \rightarrow E2$ is not) (3), fluorescence from styryl dye RH421 (4), and reactivity of the phosphorylated Asp to hydroxylamine (5). In addition, all nine cardiotonic steroids (CTSs) examined in our previous study (6) showed higher affinity in $E2P^{ATP}$ than in $E2P^{Pi}{\cdot}Mg^{2+}$. Crystal structures of NKA have been published for the $E2P^{Pi}{\cdot}Mg^{2+}$ state stabilized by various CTSs (6, 8, 9), including ouabain (OBN) and istaroxime (IST) (6), but none for the $E2P^{ATP}$ state with or without CTSs. Previous efforts to obtain crystals of NKA in $E2P^{ATP}$(CTS) were unsuccessful, but we thought cryoelectron microscopy (cryo-EM) may be applicable.

Here we demonstrate that cryo-EM is indeed successful and describe structures of NKA in the two E2P states, with and without OBN or IST. IST was selected because of its different chemical structure from conventional CTSs, such as OBN, and because it is reported to have great potency in clinical use (10). To our surprise, the electron microscopy (EM) maps for the $E2P^{ATP}$ state are rather good even without stabilization by a CTS, and differences between the two E2P states are evident at the transmembrane metal binding site M. In $E2P^{Pi}$, we see strong density at site M attributable to

Author affiliations: [a]Institute for Quantitative Biosciences, The University of Tokyo, Bunkyo-ku, Tokyo 113-0032, Japan; and [b]Department of Biomedicine, Aarhus University, 8000 Aarhus C, Denmark

Author contributions: R.K. and C.T. designed research; R.K., F.C., B.V., and C.T. performed research; R.K. and C.T. analyzed data; and R.K., F.C., B.V., and C.T. wrote the paper.

Reviewers: K.A., Nagoya Daigaku; and K.S., Massachusetts General Hospital.

The authors declare no competing interest.

[1]To whom correspondence may be addressed. Email: ct@iqb.u-tokyo.ac.jp.

This article contains supporting information online at http://www.pnas.org/lookup/suppl/doi:10.1073/pnas.2123226119/-/DCSupplemental.

Published April 5, 2022.

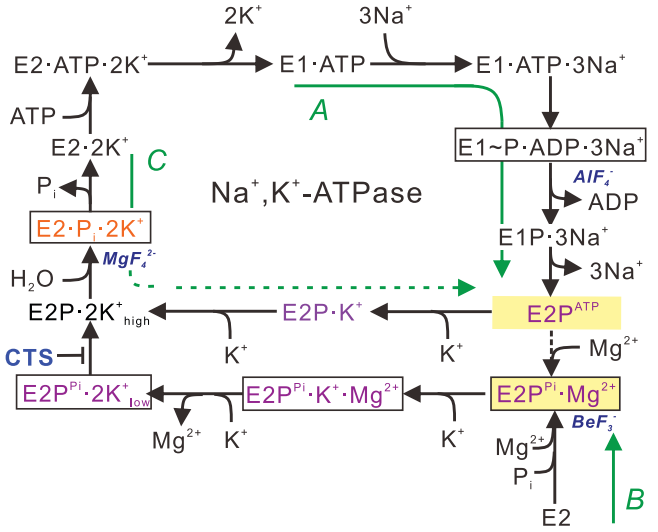

Fig. 1. A reaction diagram of NKA with special emphasis on the two E2P states, $E2P^{ATP}$ and $E2P^{Pi}{\cdot}Mg^{2+}$. $E2P^{ATP}$ is the physiological E2P ground state (path A); $E2P^{Pi}{\cdot}Mg^{2+}$ can be formed in the backward reaction starting from E2 with P_i (path B). Phosphorylation reaction requires Mg^{2+} at the phosphorylation site of NKA but incorporates another Mg^{2+} at site M, a transmembrane binding site for Mg^{2+}, in $E2P^{Pi}{\cdot}Mg^{2+}$ (3). An $E2P^{ATP}$-like state can be formed by the backward reaction starting from $E2{\cdot}2K^+$ (path C); CTSs may stabilize a state with two K^+ bound with low affinity ($E2P^{Pi}{\cdot}2K^+_{low}$). The states that would allow high-affinity binding of CTSs appear in purple letters, and those supposed to allow low-affinity binding appear in orange letters. Crystal structures available are boxed, and phosphate analogs used are shown below the boxes. Cryo-EM structures obtained in this study are highlighted (yellow boxes). PDB IDs for published crystal structures are (limited to those related to this study) $E1{\sim}P{\cdot}ADP{\cdot}3Na^+$, 3WGU; $E2P^{Pi}{\cdot}Mg^{2+}$, 7D91; $E2P^{Pi}{\cdot}Mg^{2+}$(OBN), 7WYT; $E2P^{Pi}{\cdot}Mg^{2+}$(IST), 7WYS; $E2P^{Pi}{\cdot}Mg^{2+}$(BUF), 7DDL; $E2P^{Pi}{\cdot}Mg^{2+}{\cdot}K^+$(BUF), 7D94; $E2P^{Pi}{\cdot}2K^+$(BUF), 4RES; $E2{\cdot}P_i{\cdot}2K^+$, 2ZXE; and $E2{\cdot}P_i{\cdot}2K^+$(OBN), 3A3Y.

Mg^{2+}, as expected from the X-ray structure (6), but the map for $E2P^{ATP}$ is devoid of such density. In $E2P^{ATP}$(IST), the cation binding cavity is instead filled by the aminoalkyloxime group attached to one end of the steroid ring of IST. That is, IST in $E2P^{ATP}$ binds upside down compared to the orientation in the $E2P^{Pi}{\cdot}Mg^{2+}$(IST) crystal structure (6). The EM maps allow us to describe structural features of NKA that were unnoticed in previous X-ray structures (11, 12) and indicate that several corrections need to be made in previous atomic models. Indeed, mobile parts are resolved substantially better in the EM maps, including sugars sticking out from the β-subunit (11, 12) and many phospholipid molecules surrounding NKA.

Results and Discussion

Cryo-EM of NKA in the Two E2P States. As the source of NKA for cryo-EM, we chose the enzyme from shark rectal gland, as it withstands potential denaturation caused by detergents, such as $C_{12}E_8$, better than that from pig kidney (13). As the enzyme was solubilized with a minimal amount of detergent, most of the first-layer phospholipids and cholesterol are retained, yielding mostly dimers, consistent with a previous report (13). These dimers are artificial ones, as the protomers orient in opposite directions with respect to the membrane plane (Fig. 2*A*), as found in previous crystal structures (6, 9). Averaging of the two protomers using the twofold symmetry improved the resolution. EM maps were obtained for six structures: $E2P^{ATP}$ and $E2P^{Pi}{\cdot}Mg^{2+}$ with and without CTSs (OBN and IST). The resolution was better than 3.9 Å (*SI Appendix*, Table S1). The best resolution (3.0 Å) was obtained with $E2P^{Pi}{\cdot}Mg^{2+}$(OBN).

Structure of NKA in $E2P^{Pi}{\cdot}Mg^{2+}$ with and without OBN by Cryo-EM. The atomic model for $E2P^{Pi}{\cdot}Mg^{2+}$(OBN) obtained by cryo-EM with the shark enzyme was very similar to that obtained by X-ray crystallography for the pig kidney enzyme [Protein Data Bank (PDB) identifier (ID): 7WYT (6)]. They are superimposable (rmsd = 1.1 Å). When aligned with the M7-M10 helices, we notice slight differences in the orientation of the cytoplasmic headpiece, consisting of the A (actuator), N (nucleotide binding), and P domains, and likewise in the paths of the M1-M2 helices (*SI Appendix*, Figs. S1*A* and S2*A*). As a result, the binding cavity for CTSs is slightly narrower in the crystal structure. These differences presumably reflect packing constraints in the crystals.

As to the coordination of Mg^{2+}, EM maps are consistent with the previous atomic models obtained by X-ray crystallography. They show a density peak of 12.3σ at site M with an appropriate size for Mg^{2+} and associated water molecules (Fig. 3). However, as carboxyl groups of Asp and Glu are not well resolved in the EM maps, presumably reflecting their negative charges (14), it was impossible to be more precise. The density peak representing Mg^{2+} appears identical between 100 and 8 mM Mg^{2+}, consistent with the reported affinity for Mg^{2+} in $E2P^{Pi}{\cdot}Mg^{2+}$ [~0.5 mM (3)].

Nevertheless, it is evident that EM maps are superior in resolving mobile parts of the structure compared with X-ray electron density maps. For instance, the cytoplasmic part of the β-subunit of shark enzyme, which was not well resolved in the crystal structure (11), and the C-terminal cytoplasmic part of FXYD10 could be traced better (*SI Appendix*, Fig. S3). What is interesting is that the cytoplasmic part of FXYD10 appears to extend away from the main body of NKA, presumably to an adjacent NKA molecule. This coincides with a cross-linking experiment that reports a short distance between the C-terminal residue (Cys74) of FXYD10 and Cys249 (in shark numbering) on the A domain (15).

As we minimized the amount of detergent, most of the first-layer phospholipids are retained and well resolved (14 molecules per protomer) (*SI Appendix*, Fig. S3), but in many of them, the head groups are not. They appear as connected columns running perpendicular to the membrane plane, reflecting the negative charges of the phosphate groups (14). Cholesterol molecules are also resolved at the same locations as identified in the crystal structures (11, 12). Only one additional cholesterol molecule is newly identified.

Four sugar chains hanging from the β-subunit at four Asn residues (Asn114, Asn159, Asn194, and Asn267 in shark numbering) appear conspicuous (Fig. 2*A* and *SI Appendix*, Fig. S4). Two sugar chains have also been identified with the pig kidney enzyme at Asn158 and Asn265 (pig numbering) by X-ray crystallography (12), but here they can be traced substantially better. In two of them, the sugar chain is branched at the second residue, indicating that it is fucosylated. An extra sugar chain at Asn114 sticking out from the side of the β-subunit is identified here, specific to the shark enzyme.

Structure of NKA in $E2P^{ATP}$. It was possible to obtain well-resolved EM maps (3.4-Å resolution) for NKA in $E2P^{ATP}$ without stabilization by CTSs. The structure clearly represents an E2P state, as the overall structure is virtually identical to that of $E2P^{Pi}{\cdot}Mg^{2+}$, including the paths of the M1 and M2 helices (Fig. 2*B* and *SI Appendix*, Figs. S1*B* and S2*B*), except for details around site M, the transmembrane Mg^{2+} binding site (Fig. 2*D*). In $E2P^{ATP}$, site M is devoid of strong density that can be attributed to Mg^{2+}, irrespective of the presence or absence of

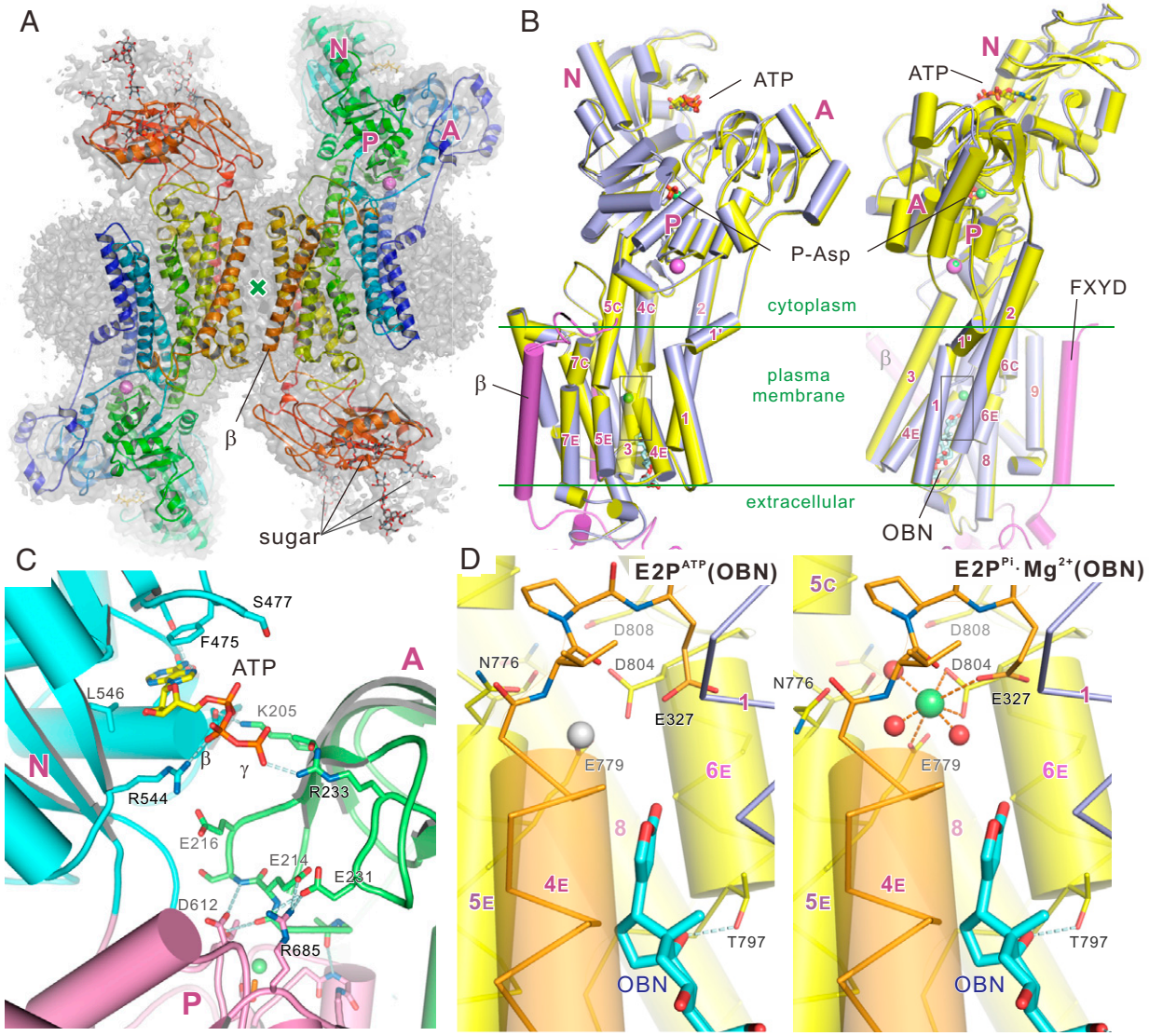

Fig. 2. Cryo-EM structures of NKA from shark rectal gland in $E2P^{ATP}$ and $E2P^{Pi}{\cdot}Mg^{2+}$. (*A*) Diprotomers of NKA in $E2P^{Pi}{\cdot}Mg^{2+}$ stabilized with OBN, consisting of the α- and β-subunits and FXYD10, viewed along the twofold axis (a small "x" at the center of the diprotomers). The three cytoplasmic domains (A, N, and P) are marked. The color of the ribbon model changes gradually from blue (*N* terminus) to red (*C* terminus). Sugar residues appear in ball and stick. (*B*) Superimposition of the atomic models for NKA in $E2P^{ATP}$ and $E2P^{Pi}{\cdot}Mg^{2+}$(OBN). Yellow, $E2P^{ATP}$; blue gray, $E2P^{Pi}{\cdot}Mg^{2+}$(OBN). P-Asp stands for the phosphorylated Asp. (*C*) ATP bridging the A and N domains in $E2P^{ATP}$. E214 is a residue in the TGES signature sequence in the A domain; D612 is in the TGD motif in the P domain. Refer to *SI Appendix*, Fig. S6*B*, for density maps around ATP. (*D*) Enlarged views of the boxed area in *B*, showing the transmembrane Mg^{2+} binding site and OBN in $E2P^{ATP}$ and $E2P^{Pi}{\cdot}Mg^{2+}$. Small green spheres represent Mg^{2+} observed in $E2P^{Pi}{\cdot}Mg^{2+}$; gray transparent ones represent putative Na^{+} in $E2P^{ATP}$. Gray dotted lines represent likely hydrogen bonds; orange ones represent coordination of Mg^{2+}. Residue numbers refer to those in pig α1. Add seven for the corresponding residue number in shark α1.

CTSs (Fig. 3 and *SI Appendix*, Fig. S5). The phosphorylation site in the P domain can be nicely modeled as a phosphorylated Asp residue with Mg^{2+} and two associated water molecules (*SI Appendix*, Fig. S6*A*).

An unexpected observation here is that ATP bridges the A and N domains (Fig. 2*C* and *SI Appendix*, Fig. S6*B*). During the transition from $E1{\cdot}ATP{\cdot}3Na^{+}$ into E2P, the tightly closed headpiece, in which the N and P domains are cross-linked by ATP/ADP (12), is thought to open on the release of ADP. Indeed, the N and P domains are now well separated (*SI Appendix*, Fig. S7), making the adenine binding site on the N domain available to ATP again but in a different geometry (*SI Appendix*, Fig. S8). The adenine ring forms a stacking interaction with Phe475/482 (pig/shark numbering) as in $E1{\cdot}AlF_4^{-}{\cdot}ADP{\cdot}3Na^{+}$ (12), but the geometry of stacking is not ideal or flanked by Leu546/553, because the adenine ring is rotated 90° with respect to the ribose. Accordingly, the side chain of Phe475/482 is rotated 90° at the Cβ atom. In $E1{\cdot}AlF_4^{-}{\cdot}ADP{\cdot}3Na^{+}$, the adenine ring is stabilized at the amino group at position 6 by salt bridges with both Asp443/450 and Glu446/453 but only with Glu446/453 in $E2P^{ATP}$. This amino group is reported to be a key component for the high affinity of ATP (0.24 μM), and its conversion to carbonyl (i.e., inosine triphosphate) reduces the affinity 1,500-fold (16). The ribose hydroxyl is stabilized by Arg685/692 in $E1{\cdot}AlF_4^{-}{\cdot}ADP{\cdot}3Na^{+}$ but not here, suggesting that the affinity for ATP is low, although the β- and the γ-phosphates form salt bridges with Arg544/551 (N domain) and Arg233/240 (A domain), respectively. Thus, ATP cross-links the N and P domains in $E1{\cdot}AlF_4^{-}{\cdot}ADP{\cdot}3Na^{+}$ (12), whereas it is the N and A domains here (Fig. 2*C*).

The β-strands around Phe475/482 are somewhat distorted and pulled toward the A domain compared to those in the $E1{\cdot}AlF_4^{-}{\cdot}ADP{\cdot}3Na^{+}$ crystal structure (12), apparently to allow ATP binding (*SI Appendix*, Fig. S8). Yet the N-domain

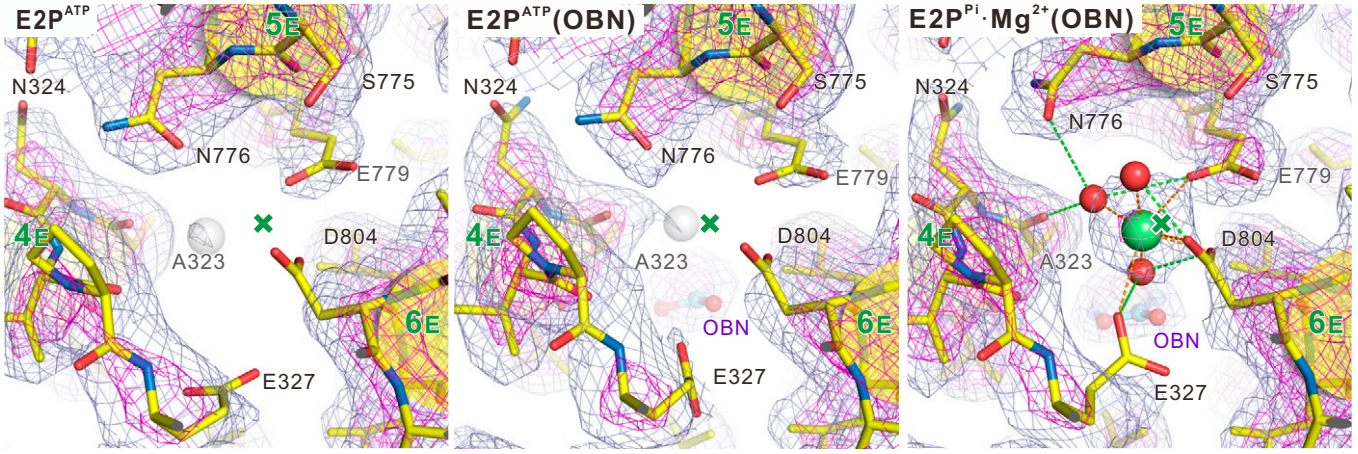

Fig. 3. Densities at site M, the transmembrane binding site for Mg^{2+}, in $E2P^{ATP}$, $E2P^{ATP}$(OBN), and $E2P^{Pi}{\cdot}Mg^{2+}$(OBN). Cryo-EM density maps (gray, 5σ; violet, 10σ) viewed from the cytoplasmic side approximately perpendicular to the membrane. The density at site M is strong (12.3σ) in $E2P^{Pi}{\cdot}Mg^{2+}$(OBN) but weak (~3.7σ) in $E2P^{ATP}$. The green sphere represents Mg^{2+}, and red ones are associated water molecules. Gray transparent spheres identify density peaks (5.0 to 5.6σ) near the Ala323 carbonyl, possibly representing Na^{+}. Green crosses specify the location of Mg^{2+} in the crystal structure of $E2P^{Pi}{\cdot}Mg^{2+}$(OBN). Its position is not exactly the same as that in the EM structure, presumably reflecting the narrower ion binding cavity in the crystal structure (*SI Appendix*, Fig. S2). Dotted lines in light green represent likely hydrogen bonds, and those in orange represent coordination of Mg^{2+}. Stereo pictures are provided in *SI Appendix*, Fig. S5. Residue numbers refer to those in pig α1. Add seven for the corresponding residue number in shark α1.

structure, including those distorted β-strands and even the orientation of the Phe475/482 side chain, is identical to that in $E2P^{Pi}{\cdot}Mg^{2+}$ with or without OBN/IST (*SI Appendix*, Fig. S7). Furthermore, a salt bridge between Lys205/212 (A domain) and Asp443/450 (N domain) stabilizes the A-N interface both in $E2P^{ATP}$ and in $E2P^{Pi}{\cdot}Mg^{2+}$ (Fig. 2*C* and *SI Appendix*, Fig. S8). When ATP is absent, as in $E2P^{Pi}{\cdot}Mg^{2+}$, another salt bridge between Glu216/223 (A domain) and Arg544/551 (N domain), which is disrupted by ATP, stabilizes the interface.

We observed no ATP molecule attached to the N domain in any other E2P species of NKA. It is unexpected that ATP stabilizes the compact headpiece here, because ATP (also ADP) is well known to accelerate K^{+} release from NKA in $E2{\cdot}2K^{+}$ (17), supposedly by destroying the compact headpiece realized in $E2{\cdot}2K^{+}$ (11). However, it is documented (18) that ATP can bind to $E2P^{Pi}$ and slow down the release of P_i with an apparent $K_{0.5}$ of 0.2 mM both in the presence and absence of OBN. Indeed, the arrangement of the A and N domains, the orientation of the Phe475/482 side chain, etc., are identical between the two E2P states (*SI Appendix*, Fig. S7).

It is worth noting in this regard that in SERCA, ATP binds to both the E2P ground state and the E2~P transition state and accelerates the dephosphorylation reaction. This is because ATP binds with higher affinity to E2~P and stabilizes it more than E2P. This effect of ATP on the dephosphorylation reaction is reversed when residues bridging the A and N domains in E2~P are mutated. That is, the E2P ground state becomes relatively more stabilized by ATP than E2~P, and the dephosphorylation reaction is slowed down (19, 20).

Binding Mode of OBN. In EM maps of NKA in $E2P^{Pi}{\cdot}Mg^{2+}$(OBN) (*SI Appendix*, Fig. S9), we see clear density representing OBN at the position expected from the previous crystal structures (6, 9). Yet the map also indicates that the orientation of the lactone ring should be flipped from that in the previous atomic models. Re-examination of the electron density maps by X-ray (PDB ID: 7WYT) supports the revised orientation. Even R factors decreased slightly. In the previous atomic model, two oxygen atoms on the lactone ring form hydrogen bonds with a water molecule associated with Mg^{2+}. After inversion, the lactone ring only fills the space created by hydrated Mg^{2+} and NKA, without forming hydrogen bonds. The electron density map for digoxin [figure 5 of (6)] also supports the revised orientation of the lactone ring. Thus, all the atomic models so far published for the complexes of NKA and CTSs with five-membered lactones (6, 8, 9) may need to be reconsidered.

Cryo-EM structures of $E2P^{ATP}$ and $E2P^{ATP}$(OBN) show hardly any differences (*SI Appendix*, Figs. S1*C* and S2*C*), indicating that the mechanism of binding of OBN to NKA in $E2P^{ATP}$ is conformational selection (21) rather than induced fit, as we proposed for CTS binding to NKA in $E2P^{Pi}{\cdot}Mg^{2+}$ (6). As depicted in Fig. 4, the binding mode of OBN to NKA and disposition of residues coordinating Mg^{2+} in $E2P^{ATP}$ show hardly any difference from those in $E2P^{Pi}{\cdot}Mg^{2+}$, although Mg^{2+} is absent in $E2P^{ATP}$ (Fig. 3 and *SI Appendix*, Fig. S5). This means that more space is available around the carbonyl group on the lactone ring in $E2P^{ATP}$. A higher affinity for any CTS in $E2P^{ATP}$ than in $E2P^{Pi}{\cdot}Mg^{2+}$ (6) will then mean that Mg^{2+} bound in $E2P^{Pi}{\cdot}Mg^{2+}$ hampers CTS binding, presumably by van der Waals repulsion. This idea is consistent with the lack of hydrogen bonds between the carbonyl group on the lactone ring and water molecules associated with Mg^{2+} in the revised model (*SI Appendix*, Fig. S9), as the difference in affinity is rather small (~1.4×) for CTSs with five-membered lactones. This number corresponds to ΔG of ~0.2 kcal/mol, much smaller than that for a hydrogen bond (>1 kcal/mol).

Binding Mode of IST. In the crystal structure of $E2P^{Pi}{\cdot}Mg^{2+}$(IST) (PDB ID: 7EVX), IST binds to NKA so that the carbonyl group at C17 on the steroid ring extends toward the extracellular side (6). This statement still holds (Fig. 4 and *SI Appendix*, Fig. S10), although we had to revise the atomic model of the complex due to two errors in chirality in the atomic model of IST. In the revised model (PDB ID: 7WYS), the amine in the aminoalkyloxime group forms a hydrogen bond with the Glu115/122 carboxyl and the Glu116/123 main chain carbonyl at the extracellular end of M1. As IST can be regarded as a derivative of digitoxin (22), it appears reasonable that IST binds to NKA in the same way as digitoxin does.

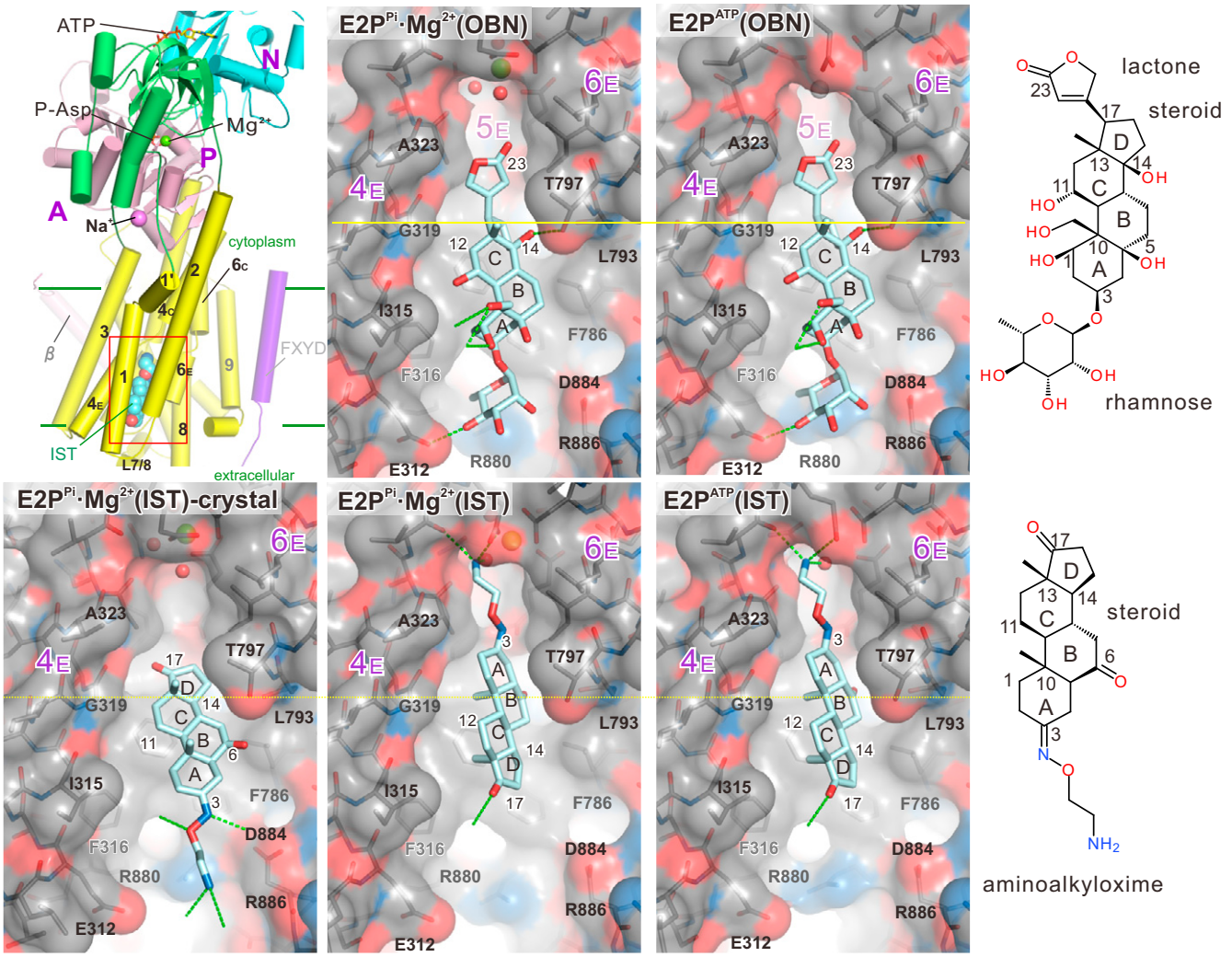

Fig. 4. Binding modes of OBN and IST in the two E2P states. The van der Waals surface of NKA in atom color is superimposed with the respective atomic models. The area enclosed by the red box in the *Upper Left* [representing $E2P^{ATP}$(IST)] is viewed parallel to the membrane. The M1 and M2 helices are removed. Chemical structures of OBN and IST are illustrated in the *Right* margin. The structure labeled $E2P^{Pi}$·Mg^{2+}(IST) crystal is derived by X-ray crystallography published previously (6) with the corrected model for IST. All the others are obtained by cryo-EM. A green sphere near the *Top* of each panel in $E2P^{Pi}$·Mg^{2+}(OBN) and $E2P^{Pi}$·Mg^{2+}(IST) represents bound Mg^{2+}, and red spheres are associated water molecules. A gray transparent sphere in $E2P^{ATP}$(OBN) identifies a density peak near the Ala323 carbonyl, possibly representing Na^+. Yellow horizontal lines show the position of the hydroxyl oxygen in Thr797; green dotted lines likely show hydrogen bonds. The density maps for OBN and IST are provided in *SI Appendix*, Figs. S9 and S10. Note that the steroid ring in IST is fairly flat, different from the chair configuration of that in OBN. Residue numbers refer to those in pig α1. Add seven for the corresponding residue number in shark α1.

To our surprise, in EM maps of NKA in $E2P^{ATP}$(IST) (*SI Appendix*, Fig. S10), we observe density extending from the main body of IST into the cation binding cavity; the other end of IST facing the extracellular medium is blunted. The density is well explained if we place IST upside down so that the aminoalkyloxime group attached to the C3 of the steroid ring extends into the cation binding cavity. In this configuration, the primary amine in the aminoalkyloxime group reaches the cluster of oxygen atoms coordinating Na^+ and K^+ at site II (Fig. 4 and *SI Appendix*, Fig. S11). Indeed, it appears to form hydrogen bonds with the Glu327/334 carboxyl and Val325/332 carbonyl oxygen. No density potentially representing a metal ion is observed. On the other end of the steroid ring, the carbonyl group on the C17 forms a hydrogen bond with the side chain of Gln111/118 on M1 (*SI Appendix*, Fig. S10). These hydrogen bonds explain the fourfold higher affinity of IST to NKA in $E2P^{ATP}$ than in $E2P^{Pi}$·Mg^{2+} (6). As the aminoalkyloxime group was introduced as a replacement of the lactone ring attached to C17 (23), this configuration is likely to be that intended.

In contrast to OBN, IST goes deeper into NKA in $E2P^{ATP}$ than OBN (Fig. 4 and *SI Appendix*, Fig. S12). The D-ring of IST overlaps with the B-ring of OBN, not the A-ring. In both IST and OBN, the stacking interaction between the steroid ring and Phe783/790 of NKA appears to be the major one. IST can go deeper into the binding site because it has a fairly flat steroid ring (22), different from the chair configuration typical of conventional CTSs, and a reduced number of side chains (only two methyl groups) sticking out from the plane of the steroid ring, free from steric constraints posed by a complex protein surface.

We surmised that in $E2P^{Pi}$·Mg^{2+}, the bound Mg^{2+} would clash sterically with the aminoalkyloxime group and prevent this binding mode of IST. Therefore, it was totally unexpected that the EM map of IST in $E2P^{Pi}$·Mg^{2+} indicates that the orientation of IST is the same as in $E2P^{ATP}$ (Fig. 4 and *SI Appendix*, Fig. S12). We tentatively place the atomic model of IST as in $E2P^{ATP}$(IST), although the density at site M (8.4σ) in $E2P^{Pi}$·Mg^{2+}(IST) is weaker than that in $E2P^{Pi}$·Mg^{2+}(OBN)

(12.3σ). There are several possibilities that can explain the difference between the crystal and EM structures. Firstly, the source of protein is different: pig kidney enzyme is used in the crystal structure analysis (6), whereas shark rectal gland enzyme is used in the EM study here. Gln119 that forms a hydrogen bond with the aminoalkyloxime group in the crystal structure is specific to pig α1. The corresponding residue in the shark enzyme is Ala126, reducing the affinity in that binding mode. Secondly, the binding cavity for IST is narrower in the crystal structure (*SI Appendix*, Fig. S2) presumably due to crystal packing. As a result, if we place IST in the same way as that in the EM structure, the steroid ring clashes with Ala323/330, where the binding cavity becomes most constricted (Fig. 4). In fact, the distance between the Ala323/330 Cβ and Thr797/804 Cγ1 is shorter by 0.8 Å in the crystal structure (*SI Appendix*, Fig. S10).

The structure of the NKA-IST complex in $E2P^{ATP}$, the physiological E2P state, easily explains many outstanding features of IST analogs described by Gobbini et al. (22). For instance, they report that the introduction of two methyl groups at the α-position to the amine reduced potency 260 times but that the introduction at the β-position produced a compound five times more potent than IST. This is well explained by the present structure, because two methyl groups would fill the space around Ile800/807 and Leu801/808 if introduced at the β-position but would clash with Val325/332 and Glu327/334 at the α-position. Replacement of the amino group with a guanidinyl group causes clashes with Asp804/811 or Asp808/815 instead of making salt bridges. This will nicely explain the ∼100 times drop in activity.

Difference in K^+ Sensitivity of the Two E2P Forms in the Dephosphorylation Reaction. Though the steady-state level of phosphorylation is ∼30% of that in the absence of K^+, the backward reaction can be used for making E2P even in the presence of K^+ (route C in Fig. 1), and the resultant E2P is dephosphorylated more rapidly when Mg^{2+} is removed (3). Also, the presence of Na^+ completely abolishes backward phosphorylation (3). Thus, whether P_i is used for phosphorylation is not the determinant of K^+ sensitivity. Indeed, according to Post et al. (3), the K^+ sensitivity changes dynamically depending on the concentrations of Mg^{2+} and Na^+. At 4 mM Mg^{2+}, the K^+-insensitive enzyme increases in time (20% after ∼20 s), even in the normal reaction cycle, but it does not do so appreciably at 0.3 mM Mg^{2+}. This effect is not saturated at 6 mM Mg^{2+} but can be reversed by increasing the Na^+ concentration from 8 to 160 mM. Indeed, we see a relatively weak density peak of about 5σ, possibly representing Na^+, near the carbonyl group of Ala323/330 (gray transparent spheres in Fig. 3 and *SI Appendix*, Fig. S5), when the Mg^{2+} concentration is low (3 mM). In contrast, even in $E2P^{ATP}$, a strong peak of about 9 σ, most likely representing Mg^{2+}, is observed at site M, when 40 mM Mg^{2+} is included (*SI Appendix*, Fig. S5). These observations are consistent with those described by Post et al. (3).

We reported that Rb^+ can bind to site I while site M is occupied by Mg^{2+} in $E2P^{Pi}{\cdot}Mg^{2+}$(bufalin [BUF]) (6). Also, in kinetic experiments with $E2{\cdot}BeF_3^-$, a stable $E2P^{Pi}$ analog, it is reported that only one Rb^+ binds to NKA in the presence of 0.3 mM Mg^{2+} (24). Thus, the binding of K^+ to site I does not cause large structural changes, but the binding to site II does. However, in E2P, only low-affinity K^+ binding to site II is possible, because the axial (perpendicular to the membrane) position of M4, which is not fully shifted to the level of that in $E2{\cdot}MgF_4^{2-}{\cdot}2K^+$, is not ideal for coordination of K^+. Movement of M4E is required for high-affinity K^+ binding to site II. Site II K^+ works as a bridge between the mobile unit for gating (M1-M3 and M4E) and the main body of the ATPase (6), and these movements of M1-M4 change the configuration of the cytoplasmic headpiece so that a water molecule is able to access the aspartylphosphate and cause dephosphorylation. This is the mechanism of acceleration of the dephosphorylation reaction by K^+. Then, the dephosphorylation reaction of NKA must critically depend on whether K^+ can bind to site II with high affinity. If Mg^{2+} has already occupied site M with relatively high affinity, K^+ binding to site II would be difficult. Moreover, M4 cannot move as it is fixed by the Mg^{2+} at site M through Glu327/334 (Fig. 2*D*). Then, site II cannot become a high-affinity binding site for K^+.

These observations suggest the following scenario. In the forward direction of the reaction cycle, the extracellular gate is closed in E1P but opens in the transition into E2P. That is, transmembrane metal binding sites are inaccessible in E1P but become accessible during the transition into E2P. Because Mg^{2+} holds water molecules much more tightly than K^+, K^+ in solution has a ∼1.5× smaller effective radius than that of Mg^{2+}, although the opposite is true in vacuum, and can move substantially faster than Mg^{2+} (25). Thus, K^+ will occupy both sites, site I first and then site II, more easily than Mg^{2+}, resulting in a K^+-sensitive enzyme. However, during many cycles of turnover, Mg^{2+} binding to site M occurs. As the bound Mg^{2+} hinders binding of K^+ to site II, the population of K^+-insensitive enzymes will increase. This generation of K^+-insensitive enzymes can be slowed down at high concentrations of Na^+ (3). In the backward phosphorylation by P_i, if started from $E2{\cdot}2K^+$, the chances for Mg^{2+} to replace K^+ would not be high, as the extracellular gate does not necessarily fully open to allow entry of Mg^{2+} and replacement of K^+. Yet as the time allowed for phosphorylation will also be much shorter due to the presence of K^+, the phosphorylation level of the enzyme will be low but with (at least partial) K^+ sensitivity. This is what is experimentally observed (3).

Difference in Accessibility of Hydroxylamine to the Acylphosphate between the Two E2P Forms. There is hardly any difference in disposition of the cytoplasmic domains between $E2P^{ATP}$ and $E2P^{Pi}{\cdot}Mg^{2+}$ (*SI Appendix*, Fig. S1*B*). Though the accessibility of hydroxylamine to the acylphosphate is biochemically different between $E2P^{Pi}{\cdot}Mg^{2+}$ and $E2P^{ATP}$ (5), we do not see any structural difference between them. As access to the acylphosphate should be prohibited in E2P, even for a water molecule (26), the distinction must be attributable to a difference in accessibility between the E2P ↔ E2 transition and the E1P ↔ E2P transition. In the E2 ↔ E2P transition, the headpiece is more compact than that in E1P ↔ E2P and does not substantially change its configuration. In contrast, the interface must open during the E1P ↔ E2P transition for ADP to leave the phosphorylation site after phosphoryl transfer, which allows hydroxylamine to gain entry, hence the difference in accessibility to the acylphosphate between the two states.

Methods

Preparation of NKA from Shark Rectal Gland. NKA was isolated from rectal glands of shark *Squalus acanthias* as described previously (11). The microsomal preparation was purified by sucrose flotation (27) and washing with ∼0.15% deoxycholate. The preparation was suspended in histidine/ethylenediaminetetraacetic acid (EDTA) buffer with 25% glycerol and kept at −80 °C until use. This preparation contained the α_1- and β_1-subunits and an equimolar amount of the FXYD10 regulatory protein (28) and showed a turnover number of 200/s at 37 °C.

For solubilized NKA, the purified membrane preparation was incubated first with 10 mM 3-morpholinopropanesulfonic acid (MOPS)–*n*-methyl-*D*-glucamine

(NMDG), pH 6.5; 25% (wt/vol) glycerol; 4 mM $MgCl_2$; and 4 mM glutathione. It was then treated with 5.2% (wt/vol) octaethyleneglycol mono-*n*-dodecylether ($C_{12}E_8$) at a weight ratio ($C_{12}E_8$/protein) of 3.5 and separated from the insoluble fraction by centrifugation at 200,000 × *g* at 10 °C. The supernatant was subjected to size-exclusion chromatography using a Superdex 200 Increase column (Cytiva) equilibrated with 1 mM $MgCl_2$, 0.01% (wt/vol) $C_{12}E_8$, 1 mM dithiothreitol, and 20 mM 2-morpholinoethanesulfonic acid–NMDG, pH 6.1, or 20 mM imidazole-HCl, pH 7.5. Peak fractions were collected and concentrated to 8 mg/mL and stored in liquid nitrogen until use.

Cryo-EM. NKA of 1.5 mg/mL was incubated for 30 min in buffers containing various ions and ligands, as listed in *SI Appendix*, Table S1, and either 20 mM MOPS-NMDG, pH 6.1, or 20 mM imidazole-HCl, pH 7.5. Then, 2.5 μL of the specimen solution was loaded onto a freshly glow-discharged Quantifoil or C-flat holey carbon grid (R1.2/1.3, Cu, 300 mesh) at 4 °C under 99% humidity and plunge frozen in liquid ethane using Vitrobot Mark IV (FEI). Images of the vitrified specimens were collected using a Titan-Krios G4 microscope (Thermo Fisher Scientific) equipped with an energy-filtered K3 detector installed at the laboratory of Dr. Kurumizaka, The University of Tokyo. Each micrograph was recorded at a pixel size of 1.08 Å with a 4.5-s exposure time, consisting of a stack of 40 frames with an accumulated total dose of ∼60 $e^-/Å^2$.

Image Analysis. All movies were aligned by MotionCor2 (29) with dose weighting. The contrast transfer function (CTF) was estimated using CtfFind4 (30). Relion 3.1 (31) was used for the following image processing. Initially, several particles of $E2P^{ATP}$(OBN) were picked manually and classified using Class2D (*SI Appendix*, Fig. S13). The averaged particle image was used for reference-based automatic picking, and the picked particles were subjected to Class2D. Three-dimensional (3D) classification was performed using the initial model generated by Relion. We obtained particle images of both protomer and diprotomer of NKA and selected those of diprotomer, as diprotomers were much more abundant than protomers and application of a twofold rotational symmetry improved the resolution of the density map. The obtained density map was used in reference-based automatic picking in the next round of processing. Finally, 1,111,500 particles were picked from 3,926 movies and 1,082,208 particles were selected after two-dimensional (2D) classification. 3D classification was performed twice, and 97,465 particles were subjected to the 3D refinement, followed by particle polishing and two rounds of CTF refinement. The final resolution of the refined density map for NKA dimers in $E2P^{ATP}$(OBN) was 3.4 Å, as estimated by the gold-standard Fourier shell correlation with the 0.143 criterion.

The density map of $E2P^{ATP}$(OBN) was used as the reference in the initial particle picking of NKA in other forms. The picked particles were subjected to 2D and 3D classifications. The initial density map was used for the next round of the reference-based picking, and the process of 2D and 3D classifications was repeated. Finally, after 3D refinement, particle polishing and two rounds of CTF refinement were carried out. The statistics of image processing are summarized in *SI Appendix*, Table S1.

Model Building and Refinement. The atomic model for NKA in $E2P^{Pi}$·Mg^{2+}(OBN) was built first on Coot (32) starting from its crystal structure (PDB ID: 7WYT) and was refined using Phenix (33). The refined structure was used as the starting model in building atomic models for other states. The statistics of the model building are summarized in *SI Appendix*, Table S1. All structure figures were prepared with PyMOL (PyMOL Molecular Graphics System, Schrödinger LLC).

Data Availability. Atomic coordinates and cryo-EM maps have been deposited in the Protein Data Bank (accession nos. 7WYU–7WZ0) and the Electron Microscopy Data Bank (accession nos. EMD-32894–EMD-32900). Refer to *SI Appendix*, Table S1, for their identities. All other study data are included in the article and/or *SI Appendix*.

ACKNOWLEDGMENTS. We are grateful to the members of the Kurumizaka laboratory, Institute for Quantitative Biosciences, The University of Tokyo, for cryo-EM data collection using the Krios G4 microscope supported by the Kurumizaka ERATO Chromatin Atlas project (JPMJER1901). As always, David B. McIntosh helped us in improving the manuscript. This work was supported in part by grants from the Danish Council for Independent Research (Grant DFF 7016-00193B to B.V. and Grant DFF4183-00011A to F.C.), the Novo Nordisk Foundation (Grant NNF14OC0013409 to B.V. and Grant NNF13OC0006555 to F.C.), the Lundbeck Foundation (Grant R223-2016-595 to B.V.), the Takeda Science Foundation (to R.K.) and the Japan Society for the Promotion of Science (KAKENHI Grant JP16H02499 to C.T. and Grant JP18K06148 to R.K.).

1. H.-J. Apell, Finding Na,K-ATPase: I – From cell to molecule. *Substantia* **2**, 17–28 (2018).
2. H.-J. Apell, Finding Na,K-ATPase II – From fluxes to ion movements. *Substantia* **3**, 19–41 (2019).
3. R. L. Post, G. Toda, F. N. Rogers, Phosphorylation by inorganic phosphate of sodium plus potassium ion transport adenosine triphosphatase. Four reactive states. *J. Biol. Chem.* **250**, 691–701 (1975).
4. F. Cornelius, N. U. Fedosova, I. Klodos, E2P phosphoforms of Na,K-ATPase. II. Interaction of substrate and cation-binding sites in Pi phosphorylation of Na,K-ATPase. *Biochemistry* **37**, 16686–16696 (1998).
5. N. U. Fedosova, F. Cornelius, I. Klodos, E2P phosphoforms of Na,K-ATPase. I. Comparison of phosphointermediates formed from ATP and Pi by their reactivity toward hydroxylamine and vanadate. *Biochemistry* **37**, 13634–13642 (1998).
6. R. Kanai *et al.*, Binding of cardiotonic steroids to Na^+,K^+-ATPase in the E2P state. *Proc. Natl. Acad. Sci. U.S.A.* **118**, e2020438118 (2021).
7. C. Toyoshima *et al.*, Crystal structures of the calcium pump and sarcolipin in the Mg^{2+}-bound E1 state. *Nature* **495**, 260–264 (2013).
8. M. Laursen, J. L. Gregersen, L. Yatime, P. Nissen, N. U. Fedosova, Structures and characterization of digoxin- and bufalin-bound Na^+,K^+-ATPase compared with the ouabain-bound complex. *Proc. Natl. Acad. Sci. U.S.A.* **112**, 1755–1760 (2015).
9. M. Laursen, L. Yatime, P. Nissen, N. U. Fedosova, Crystal structure of the high-affinity Na^+K^+-ATPase-ouabain complex with Mg^{2+} bound in the cation binding site. *Proc. Natl. Acad. Sci. U.S.A.* **110**, 10958–10963 (2013).
10. S. Aditya, A. Rattan, Istaroxime: A rising star in acute heart failure. *J. Pharmacol. Pharmacother.* **3**, 353–355 (2012).
11. T. Shinoda, H. Ogawa, F. Cornelius, C. Toyoshima, Crystal structure of the sodium-potassium pump at 2.4 Å resolution. *Nature* **459**, 446–450 (2009).
12. R. Kanai, H. Ogawa, B. Vilsen, F. Cornelius, C. Toyoshima, Crystal structure of a Na^+-bound Na^+,K^+-ATPase preceding the E1P state. *Nature* **502**, 201–206 (2013).
13. M. Esmann, Solubilized ($Na^+ + K^+$)-ATPase from shark rectal gland and ox kidney–An inactivation study. *Biochim. Biophys. Acta* **857**, 38–47 (1986).
14. K. Yonekura, K. Kato, M. Ogasawara, M. Tomita, C. Toyoshima, Electron crystallography of ultrathin 3D protein crystals: Atomic model with charges. *Proc. Natl. Acad. Sci. U.S.A.* **112**, 3368–3373 (2015).
15. Y. A. Mahmmoud, H. Vorum, F. Cornelius, Interaction of FXYD10 (PLMS) with Na,K-ATPase from shark rectal glands. Close proximity of Cys74 of FXYD10 to Cys254 in the a domain of the alpha-subunit revealed by intermolecular thiol cross-linking. *J. Biol. Chem.* **280**, 27776–27782 (2005).
16. C. Hegyvary, R. L. Post, Binding of adenosine triphosphate to sodium and potassium ion-stimulated adenosine triphosphatase. *J. Biol. Chem.* **246**, 5234–5240 (1971).
17. R. L. Post, C. Hegyvary, S. Kume, Activation by adenosine triphosphate in the phosphorylation kinetics of sodium and potassium ion transport adenosine triphosphatase. *J. Biol. Chem.* **247**, 6530–6540 (1972).
18. A. Askari, W. Huang, Na^+, K^+-ATPase: Evidence for the binding of ATP to the phosphoenzyme. *Biochem. Biophys. Res. Commun.* **104**, 1447–1453 (1982).
19. J. D. Clausen, A. N. Holdensen, J. P. Andersen, Critical roles of interdomain interactions for modulatory ATP binding to sarcoplasmic reticulum Ca^{2+}-ATPase. *J. Biol. Chem.* **289**, 29123–29134 (2014).
20. J. D. Clausen, D. B. McIntosh, D. G. Woolley, J. P. Andersen, Modulatory ATP binding affinity in intermediate states of E2P dephosphorylation of sarcoplasmic reticulum Ca^{2+}-ATPase. *J. Biol. Chem.* **286**, 11792–11802 (2011).
21. A. D. Vogt, E. Di Cera, Conformational selection or induced fit? A critical appraisal of the kinetic mechanism. *Biochemistry* **51**, 5894–5902 (2012).
22. M. Gobbini *et al.*, Novel analogues of istaroxime, a potent inhibitor of Na^+,K^+-ATPase: Synthesis and structure-activity relationship. *J. Med. Chem.* **51**, 4601–4608 (2008).
23. A. Cerri *et al.*, 17β-*O*-Aminoalkyloximes of 5β-androstane-3β,14β-diol with digitalis-like activity: Synthesis, cardiotonic activity, structure-activity relationships, and molecular modeling of the $Na(^+)$,$K(^+)$-ATPase receptor. *J. Med. Chem.* **43**, 2332–2349 (2000).
24. S. E. Faraj, M. Centeno, R. C. Rossi, M. R. Montes, A kinetic comparison between E2P and the E2P-like state induced by a beryllium fluoride complex in the Na,K-ATPase. Interactions with Rb^+. *Biochim. Biophys. Acta Biomembr.* **1861**, 355–365 (2019).
25. M. Y. Kiriukhin, K. D. Collins, Dynamic hydration numbers for biologically important ions. *Biophys. Chem.* **99**, 155–168 (2002).
26. C. Toyoshima, Y. Norimatsu, S. Iwasawa, T. Tsuda, H. Ogawa, How processing of aspartylphosphate is coupled to lumenal gating of the ion pathway in the calcium pump. *Proc. Natl. Acad. Sci. U.S.A.* **104**, 19831–19836 (2007).
27. L. R. Jones, Rapid preparation of canine cardiac sarcolemmal vesicles by sucrose flotation. *Methods Enzymol.* **157**, 85–91 (1988).
28. Y. A. Mahmmoud, H. Vorum, F. Cornelius, Identification of a phospholemman-like protein from shark rectal glands. Evidence for indirect regulation of Na,K-ATPase by protein kinase c via a novel member of the FXYDY family. *J. Biol. Chem.* **275**, 35969–35977 (2000).
29. S. Q. Zheng *et al.*, MotionCor2: Anisotropic correction of beam-induced motion for improved cryo-electron microscopy. *Nat. Methods* **14**, 331–332 (2017).
30. A. Rohou, N. Grigorieff, CTFFIND4: Fast and accurate defocus estimation from electron micrographs. *J. Struct. Biol.* **192**, 216–221 (2015).
31. S. H. W. Scheres, RELION: Implementation of a Bayesian approach to cryo-EM structure determination. *J. Struct. Biol.* **180**, 519–530 (2012).
32. P. Emsley, K. Cowtan, Coot: Model-building tools for molecular graphics. *Acta Crystallogr. D Biol. Crystallogr.* **60**, 2126–2132 (2004).
33. P. D. Adams *et al.*, PHENIX: A comprehensive Python-based system for macromolecular structure solution. *Acta Crystallogr. D Biol. Crystallogr.* **66**, 213–221 (2010).